www.sciencemag.org/cgi/content/full/336/6079/296-c/DC1

Supplementary Materials for

Comment on "Detection of Emerging Sunspot Regions in the Solar Interior"

Douglas C. Braun

E-mail: dbraun@cora.nwra.com

Published 20 April 2012, *Science* **336**, 296-c (2012)
DOI: 10.1126/science.1215425

This PDF file includes:

Materials and Methods

The analysis here uses focus depths of 45, 54, 64, and 76 Mm below the surface. Separate phase-speed filters, for each of the four depths were applied to the time-series of Doppler data. The filters are Gaussians with values of one and one-half at the highest and lowest wavenumbers respectively, at 4mHz, listed in Table 1 of (*6*), which also lists the radii of the annuli employed for each depth. A boxcar frequency filter spanning 2.5 to 5.5 mHz was also used. Travel times were extracted from correlations between the egression and ingression amplitudes using the phase method (*13*). Greens functions were computed using the the eikonal approximation in spherical coordinates (*14*). A convolution in time and in Cartesian spatial coordinates of the Greens function with the Doppler data, using Postel projections, was used as an approximation to compute the egression and ingression amplitudes (*14*). This "plane-parallel" approximation is computationally efficient but causes a spatially-varying bias, and other distortions of the travel-time-shift maps (*14*), which increase with the distance from the Postel tangent point (the plane-parallel approximation is accurate at the center of the Postel projection). These effects were minimized by placement of the Postel tangent point within a heliocentric angle of 0.07 radians of the position of the reported signatures and removing a second-order two-dimensional polynomial, in the Cartesian coordinates of the Postel projection, from each travel-time-shift map. Tests (see Fig. S1) show that the remaining effects of the distortion are acceptably small for the work discussed here. The egression-ingression correlations are computed for diametrically opposed arcs in the annulus, which have arc lengths identical to those employed for averaging the Doppler signal in the time-distance analysis of Ilonidis *et al.* (*1*). I define an "arc configuration" to be one of 20 sets of (five) arc lengths and (four) angular orientations of the arcs used by Ilonidis *et al.* (*1*). Egression-ingression correlations are computed here using the same twenty arc configurations employed in the time-distance analysis, albeit with the wider annuli specified in (*6*). Fig. 1 shows maps of the travel-time shifts averaged over the four target

depths while Fig. S2 shows maps for the individual target depths.

References and Notes

1. S. Ilonidis, J. Zhao, A. Kosovichev, *Science* **333**, 993 (2011).

2. A. C. Birch, D. C. Braun, Y. Fan, *Astrophys. J.* **723**, L190 (2010).

3. L. Gizon, A. C. Birch, H. C. Spruit, *Ann. Rev. Astron. Astrophys.* **48**, 289 (2010).

4. C. Lindsey, D. C. Braun, *Astrophys. J. Suppl.* **155**, 209 (2004).

5. D. C. Braun, A. C. Birch, D. Benson, R. F. Stein, A. Nordlund, *Astrophys. J.* **669**, 1395 (2007).

6. D. C. Braun, A. C. Birch, *Astrophys. J.* **689**, L161 (2008).

7. Materials and methods are available as supplementary material on *Science* Online.

8. P. H. Scherrer, *et al.*, *Sol. Phys.* **162**, 129 (1995).

9. L. Gizon, A. C. Birch, *Astrophys. J.* **614**, 472 (2004).

10. C. Lindsey, D. C. Braun, *Science* **287**, 1799 (2000).

11. D. C. Braun, C. Lindsey, *Astrophys. J.* **560**, L189 (2001).

12. J. Zhao, *Astrophys. J.* **664**, L139 (2007).

13. D. C. Braun, C. Lindsey, *Sol. Phys.* **192**, 307 (2000).

14. C. Lindsey, D. C. Braun, *Sol. Phys.* **192**, 261 (2000).

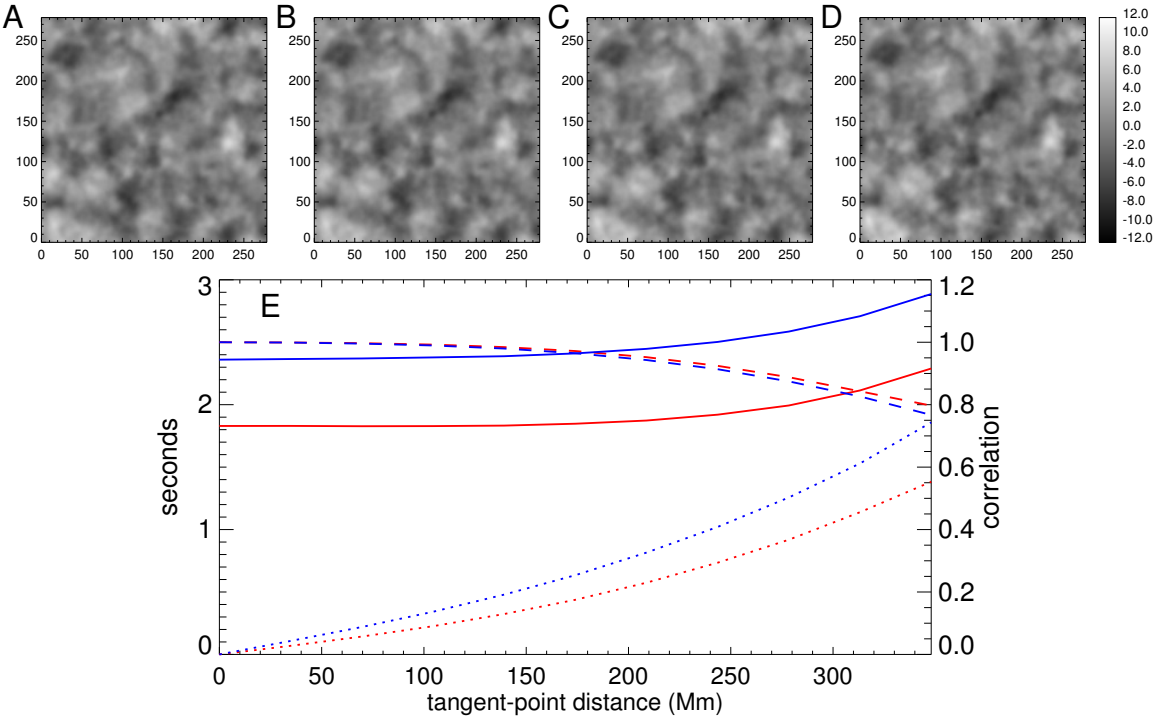

Fig. S1 A test of the distortion introduced by the use of the plane-parallel approximation, where the application of the holographic Green's function is performed using a temporal and (two-dimensional Cartesian) spatial convolution of the Green's function with the MDI Doppler data. (**A**) A portion of a depth-averaged travel-time shift map computed with 6 hours of MDI data remapped onto a Postel projection with the tangent point at the center of the frame. This example employs only a single arc configuration (with 14 arcs) of the holography annulus. The panels (**B** - **D**) show the maps for the same region but with the tangent point of the Postel projection located at increasing increments of 0.1 radians (69.6 Mm) away from the center towards the top of the page. (**E**) Quantitative comparisons of travel-time shifts in the maps made with increasing distance (horizontal axis) of the Postel tangent point from the center of the map. The solid lines show the root-mean-square (RMS) of the travel-time shifts in the given map while the dotted lines indicate the RMS of the difference between the given map and the map at zero

tangent-point distance (referenced to the left axis), and the dashed lines indicate the correlation coefficient between those maps (referenced to the right axis). The comparisons use a centered 200 Mm diameter circular portion of the maps and the red and blue colors indicate results for arc configurations with 6 and 14 arcs respectively. For the purposes of this study distances of up to 200 Mm, where the resulting RMS differs by less than a second and the maps are nearly indistinguishable by eye from the tangent-point centered map, are deemed acceptable.

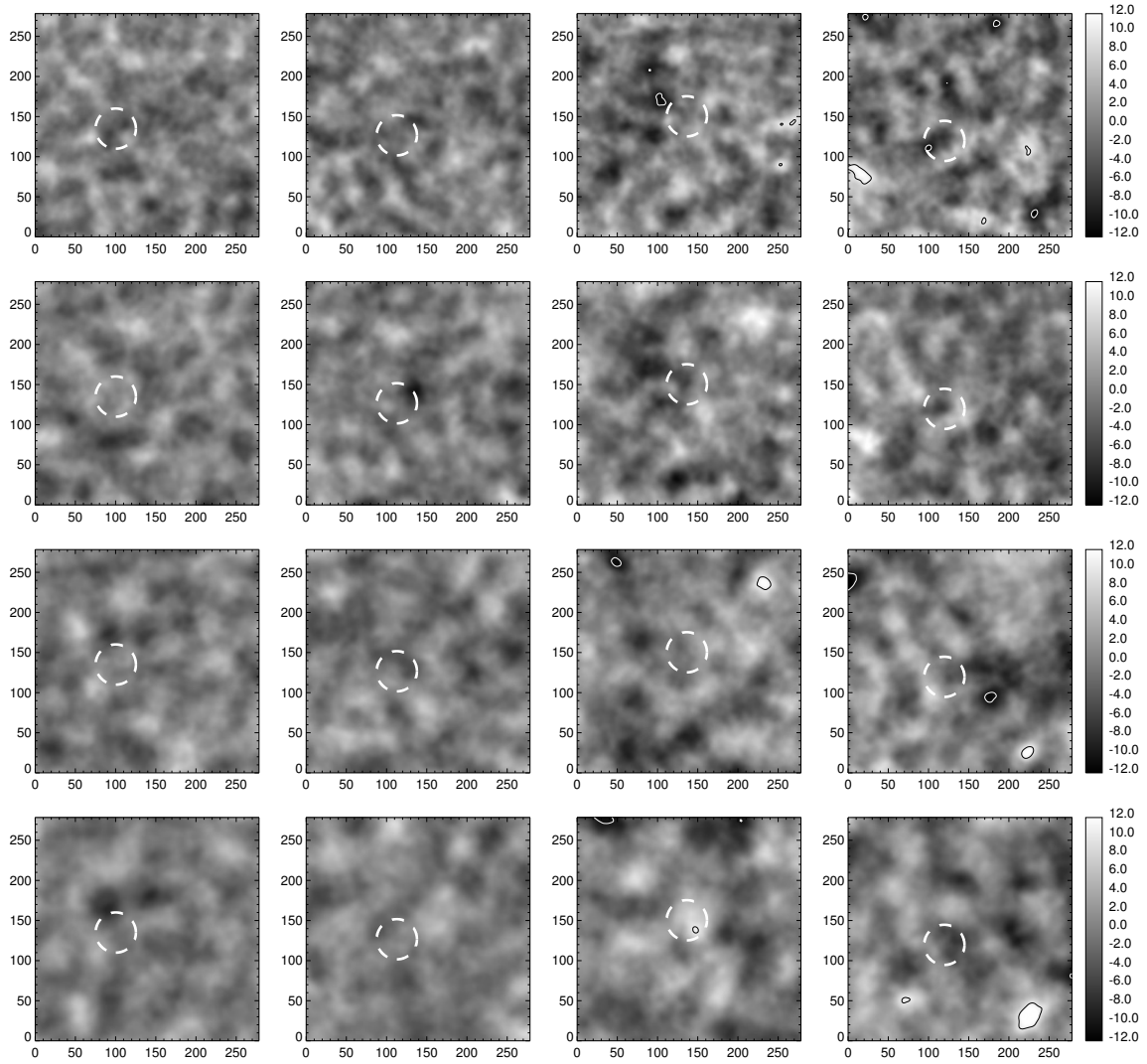

Fig. S2 Travel-time shift maps for the individual target depths. The columns indicate the four different active regions, in the same order as in Fig. 1. The rows (top to bottom) indicate depths of 45, 54, 64, and 76 Mm below the surface. The dashed circles are the same target regions shown in Fig. 1. Black (white) contours indicate travel-time shifts of +10 (-10) s. The noise is estimated to be about 3 s. The vertical distance between the target depths is smaller than the vertical wavelength of acoustic waves used in the analysis which results in a significant

correlation between the individual maps.

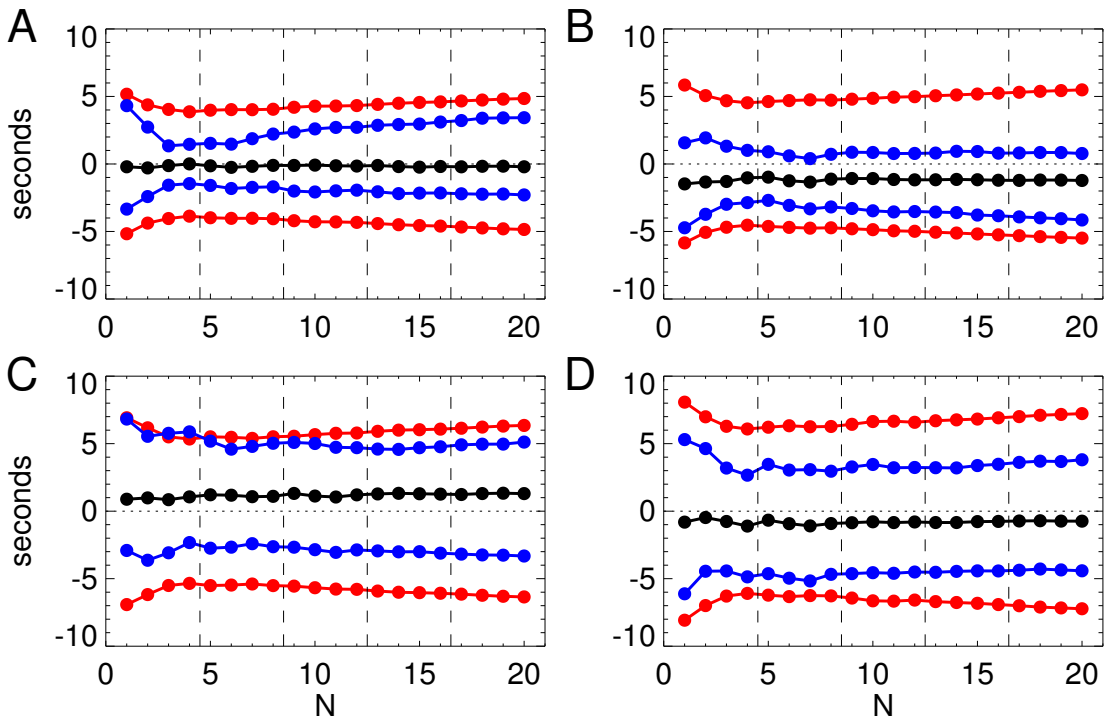

Fig. S3 Properties of the travel-time shifts within the 50 Mm diameter target regions shown in Fig. 1. Panels **A** through **D** show results for AR 07978, AR 08164, AR 08171, and AR 10488 respectively. The connected red dots indicate $\pm 3\sigma$ where the noise σ represents the RMS of the travel-time shifts over an annulus spanning 110 and 195 Mm from the center of each map. The black dots indicate the average over the target regions shown in Fig. 1, and the blue dots indicate the minimum and maximum values. The results are shown as a function of the cumulative number (N) of arc configurations which contribute to the travel-time shift determinations. The order of the arc configurations is from large to small arc lengths, such that $N = 1$ through 4 correspond to the four angular orientations of the 6-arc geometry, $N =$ 5 to 8 correspond to the four angular orientations of the 8-arc geometry, and so on, up to the 14-arc geometry (the vertical dashed lines indicate each switch to a larger number of arcs). The noise decreases as the first four configurations are used, then increases with greater N. This is

apparently the result of increasing noise in the maps made with smaller arc lengths (the noise in depth-averaged travel-time shift maps made with individual arc configurations increases from $\sim$ 2 to $\sim$ 2.7 s as the number of arcs varies from 6 to 14). For $N > 8$ there appears to be no substantial change in either the minimum, maximum, or mean value within target regions as N is increased. Fig. S4 shows examples of individual travel-time shift maps with different N. For the final maps (from correlations summed over all 20 arc configurations) the typical RMS is about $\sim$ 2 s, although differences of up to $\sim$ 0.7 s are observed between datasets. These differences appear to reflect the presence of of data gaps and possibly long-term changes in the instrument (for example, changes of focus).

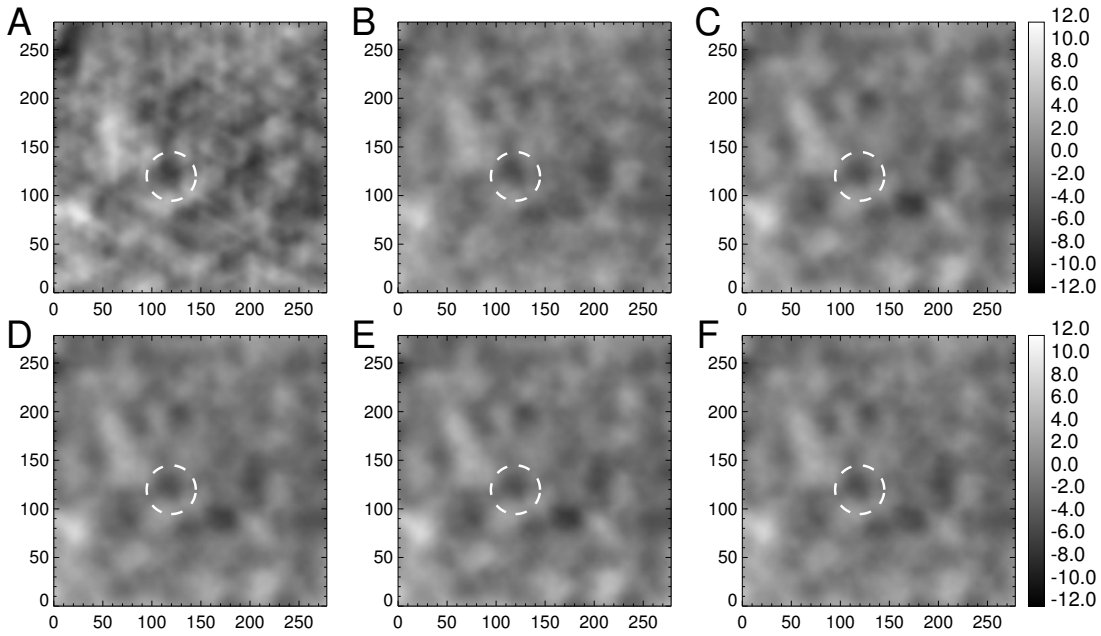

Fig. S4 Examples of travel-time shift maps as the number of arc configurations used in the analysis is increased. (**A**) The travel-time shift map for the target region below AR 10488 with just a single orientation of the 6-arc configuration (i.e. $N = 1$ in Fig.S3 averaged over the four target depths. (**B**) Averaged map for $N = 4$. (**C**) Averaged map for $N = 8$. (**D**) Averaged map for $N = 12$. (**E**) Averaged map for $N = 16$. (**F**) Averaged map for $N = 20$.